



8-2020

Experimental implementation of wavefront sensorless real-time adaptive optics aberration correction control loop with a neural network

Minhzaio Liu
Illinois Wesleyan University

David N. Lopez
Illinois Wesleyan University

Gabriel C. Spalding
Illinois Wesleyan University

Follow this and additional works at: https://digitalcommons.iwu.edu/physics_scholarship



Part of the [Physics Commons](#)

Recommended Citation

Liu, Minhzaio; Lopez, David N.; and Spalding, Gabriel C., "Experimental implementation of wavefront sensorless real-time adaptive optics aberration correction control loop with a neural network" (2020). *Scholarship*. 14.

https://digitalcommons.iwu.edu/physics_scholarship/14

This Article is protected by copyright and/or related rights. It has been brought to you by Digital Commons @ IWU with permission from the rights-holder(s). You are free to use this material in any way that is permitted by the copyright and related rights legislation that applies to your use. For other uses you need to obtain permission from the rights-holder(s) directly, unless additional rights are indicated by a Creative Commons license in the record and/ or on the work itself. This material has been accepted for inclusion by faculty at Illinois Wesleyan University. For more information, please contact digitalcommons@iwu.edu.

©Copyright is owned by the author of this document.

Experimental implementation of wavefront sensorless real-time adaptive optics aberration correction control loop with a neural network

Minzhao Liu, David N. Lopez and Gabriel. C. Spalding

Illinois Wesleyan University, Dept. of Physics, 1312 Park Street, Bloomington, IL 61701 USA

ABSTRACT

Recently, deep neural network (DNN) based adaptive optics systems were proposed to address the issue of latency in existing wavefront sensorless (WFS-less) aberration correction techniques. Intensity images alone are sufficient for the DNN model to compute the necessary wavefront correction, removing the need for iterative processes and allowing practical real-time aberration correction to be implemented. Specifically, we generate the desired aberration correction phase profiles utilizing a DNN based system that outputs a set of coefficients for 27 terms of Zernike polynomials. We present an experimental realization of this technique using a spatial light modulator (SLM) on real physical turbulence-induced aberration. We report an aberration correction rate of 20 frames per second in this laboratory setting, accelerated by parallelization on a graphics processing unit. There are a number of issues associated with the practical implementation of such techniques, which we highlight and address in this paper.

Keywords: Adaptive optics, spatial light modulator, aberration, neural network

1. INTRODUCTION

Adaptive optics (AO) utilizing deformable mirrors (DM) or spatial light modulators (SLM) have been extended in recent years to improve the performance of various optical systems, by removing phase distortions from incoming light.¹⁻³ Such systems are now used in astronomical imaging, microscopy, and free-space communication. In astronomy, it is common for the incoming wavefront to be directly measured by a wavefront sensor (WFS),⁴ but in a number of other application areas, this can become impractical; in such cases required compensation can, instead, be inferred from intensity images, which would be called a wavefront sensorless (WFS-less) approach. Conventional WFS-less techniques can be various model-free search algorithms,⁵⁻⁹ or algorithms that incorporate the expected characteristics of aberration phase profiles based upon physical models of turbulence.¹⁰⁻¹² One advantage of WFS-less aberration correction is a lower implementation cost, but a key limitation is that conventional approaches require multiple iterations or measurements for the system to converge, with each iteration or measurement supplying additional information about the aberration phase profile.⁵ Thus, one limitation of conventional WFS-less systems is that the need for iterations leads to delays, which makes them unsuitable for real-time aberration correction, a necessity for applications such as free-space communication.

The problem of finding the complex phase of light from intensity after a Fourier lens is an inverse problem that does not have deterministic solutions, since incomplete information is provided (amplitude and phase would be sufficient to find the solution by Fourier transform). However, approximate solutions can be found, and this task is suitable for a deep neural network (DNN) due to the universal approximation theorem: “a feed-forward network with a single hidden layer containing a finite number of neurons can approximate continuous functions on compact subsets of \mathbf{R}^n ...”.¹³ Previous works¹⁴⁻¹⁶ have shown, using simulation, that DNN based models can reduce aberration with millisecond latency without the need for iterations, thereby opening up a wider

Further author information:

M.L.: E-mail: mliu1@iwu.edu

D.N.L.: E-mail: dlopez1@iwu.edu

G.C.S.: E-mail: gspaldin@iwu.edu

range of applications to real-time WFS-less aberration correction. Obtaining images at different focal positions, simultaneously, provides more information, further improving the performance of the network.^{15,16}

We implemented the algorithm using an SLM for phase compensation. One challenge of implementing the DNN method lies in generating high-resolution phase profiles fast enough for real-time aberration correction even though all necessary information can be obtained from the neural network quickly, which suggests the use of a GPU for data parallelization. Here, Tensorflow, CUDA, and Numba Python libraries are used.

2. THEORY

2.1 Mathematical description of the optical system

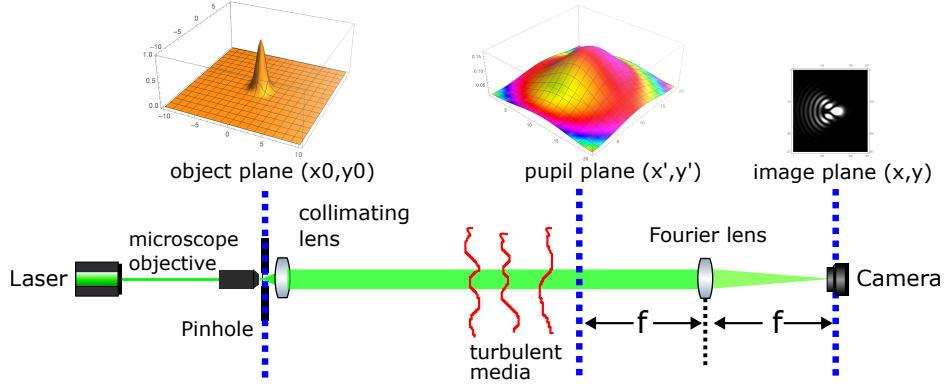


Figure 1. Unfolded schematic. At the object plane, the optical field (shown above in an intensity map) is approximately an impulse function, with uniform phase. Traversal of turbulent media yields, at the pupil plane, a complex field: the field map (shown above) shows phase distortion via a $0 - 2\pi$ color map (this example shows coma aberration). The image plane field is the Fourier transform of the pupil plane field (shown above is the amplitude of the point spread function, with coma aberration).

Fig. 1 shows the schematic of relevant optical planes and components. Let $U(x_0, y_0)$ be the field distribution in the object plane, where x_0, y_0 are transverse coordinates within that plane. In the scalar approximation, the optical field distribution at the pupil plane is completely described by an amplitude profile $A(x', y')$ and a phase profile $\Phi(x', y')$, where x', y' are the transverse position coordinates within the pupil plane. It is this phase profile that describes the wavefront aberration.

Let us denote this pupil plane field as $P(x', y')$, where:

$$P(x', y') = A(x', y')e^{ik\Phi(x', y')}, \quad (1)$$

and k is the wavenumber of the laser. Ignoring the scaling effects of our optical system, the intensity distribution on the camera is:¹⁷

$$I(x, y) = |U(-x_0, -y_0) * \mathcal{F}(P(x', y'))|^2, \quad (2)$$

where x, y are coordinates of the image plane, \mathcal{F} is the Fourier transform operator and $*$ is the convolution operator. In our case, U is taken to be an impulse function since our object is a pinhole, which simplifies our expression for I to:

$$I(x, y) = |\mathcal{F}(P(x', y'))|^2. \quad (3)$$

Zernike polynomials form a complete orthogonal basis set on the unit disk, and the first few terms describe commonly discussed aberrations in optical systems such as coma, astigmatism, etc. This makes them attractive as basis functions of our phase profiles of a Gaussian beam. Hence, our transverse phase profile will be written as:

$$\Phi(x', y') = \sum_j a_j Z_j, \quad (4)$$

where Z_j is the j th Zernike polynomial in Noll's¹⁸ convention. However, not all arbitrary phase profiles are equally likely. Energy constraints limit the characteristics of density variation associated with atmospheric turbulence. The consequence of this is that high order Zernike terms are generally weaker, and certain terms are correlated due to constraints of the Kolmogorov spectrum of turbulence.^{18,19}

Following the method described in simulations by Roddier,²⁰ we are able to generate Zernike coefficients satisfying the observed distribution. We first computed the correlation matrix \mathbf{C} of the coefficients. It can be verified that \mathbf{C} is Hermitian, and therefore there must exist a unitary matrix \mathbf{U} such that $\mathbf{U} \cdot \mathbf{C} \cdot \mathbf{U}^{-1}$ is diagonal, which gives us the correlation matrix for independent random Karhunen-Loève coefficients. A singular value decomposition is performed to find such a \mathbf{U} . A minor fix to rearrange the basis of \mathbf{C} such that the new matrix is block diagonal is performed to avoid eigenvalue problems. This allows us to generate the Karhunen-Loève coefficients first and then convert back to Zernike coefficients for simulating atmospheric turbulence.

2.2 Architecture of neural network

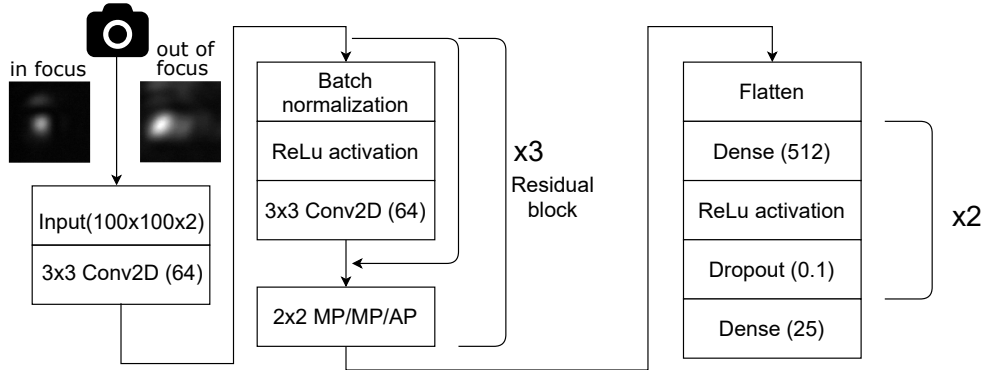


Figure 2. Neural network architecture. Each convolutional layer (Conv2D) has 64 channels of three by three filters, and uses ‘same padding’. The first two residual blocks use max pooling (MP) and the last uses average pooling (AP). Adam optimizer is used.

Details of the neural network are shown in Fig. 2. In-focus and out-of-focus images are simultaneously captured, on different regions of a single camera. The neural network takes camera intensity images as the input. In order to extract information about different image features, filter matrices are convolved with 2D image data in convolutional layers (Conv2D). One convolutional layer is applied immediately after the input, and three more are embedded in three residual blocks. In each residual block, the input of the block is added to the end of the convolutional layer. This allows each block to skip some intermediary connections and the gradient to propagate back efficiently, tackling the vanishing gradient problem. In the end, fully connected layers are used to convert feature information into Zernike coefficients. The architecture of the neural network closely follows the aforementioned simulation work from Moerner’s group.¹⁶ However, there are three aspects of our network that are different: our input is simplified to consist of images at two focal positions instead of five; our image size is 100 by 100; and we are interested in the first 28 Zernike coefficients. Since the first Zernike term is an overall (piston) phase shift and has no effect here, and the second and third are tip and tilt terms that can be easily estimated using other methods, the output layer of our network has 25 neurons for 25 coefficients.

There are a number of issues associated with the practical implementation of such techniques, which we highlight and address in this paper. In reality, the neural network is very sensitive to any change in the data set. For example, if the overall intensity of the images acquired for testing differs from that of the training data set, the performance of the network degrades significantly. To make our network insensitive to these changes, acquired images are centered and cropped and the overall intensity is normalized, i.e. image intensities are divided by the sum of pixel values and multiplied by a fixed factor to compensate for the division.

2.3 Theory of aberration correction control

To perform aberration correction, the system first acquires an image with the camera, then feeds the image to the neural network, which outputs Zernike coefficients. These coefficients are fed into the GPU algorithm to compute the correction phase profile and, given the limited phase throw possible on an SLM, displays a phase-wrapped version of the resulting phase profile on the SLM. After one iteration of correction, a second image is acquired by the camera. So long as the frame rate of aberration correction is higher than the characteristic rate of temporal turbulence variation, the system should be able to reduce aberration.

The next acquired image would have the effects of the previous iteration of aberration correction, so the Zernike coefficients obtained from this image should be added to the previous set of Zernike coefficients, and the phase profile should be computed accordingly. As time goes on, the validity of previously obtained aberration profiles decreases because the aberration would have changed. This means that part of the optimization process involves the determination of a factor that multiplies the previous phase profile. For this reason, we give exponentially decreasing weights to previous phase profiles. These considerations make real-time aberration correction a closed-loop control problem.²¹

The modified control function is:

$$\vec{u}(t) = K_p \left\{ \vec{e}(t) + \frac{1}{T_i} \int_0^t \vec{e}(t') \text{Exp}[-\lambda(t - t')] dt' \right\}, \quad (5)$$

where \vec{u} is the set of Zernike coefficients for aberration correction, \vec{e} is the set of estimated errors in Zernike coefficients, and K_p, T_i are gain and integration time, respectively. λ is the decay in the effect of previous errors. In most adaptive optics control systems, the decay term is not used.²¹ The decay term proved to be useful in our application to mitigate large curvatures around the edge of the correction profile where effects are not strong due to lower light intensity, as imperfect estimates of correction coefficients can conspire to give a flat profile at the center but accumulate steep phase changes on the edge.

In the computer algorithm, the control is implemented in the following way:

$$\vec{u}(j) = K_p \left\{ \vec{e}(j) + \frac{1}{T_i} \vec{E}(j) \right\} \quad (6)$$

$$\vec{E}(j) = D \vec{E}(j-1) + \vec{e}(j-1), \quad (7)$$

where j is the frame number, \vec{E}_j reflects, for the j th frame, the (exponentially) weighted sum of previous errors, and D is a multiplicative constant leading to the decay, related to λ .

3. EXPERIMENT

3.1 Experimental setup

A schematic of our experiment is shown in Fig. 3. A 532 nm green diode laser beam is used, which is spatially filtered (pinhole is at the object plane) and expanded such that most of the intensity of the beam is contained by a 1920×1080 Jasper Display JD955B SLM. The input polarizer and output analyzer of the system are rotated such that the SLM operates in pure phase modulation mode. The SLM is positioned at the pupil (back focal) plane of a lens of focal length 750 mm, and a Prosilica EC1280 firewire camera is positioned at the image (front focal) plane.

To add physical aberration, the laser is passed through a water tank. A thermoelectric (T.E.) device is placed in water to create density variation as well as slow currents, and a motorized water propelling system is used to create fast currents if desired. Salt is added to allow further density variation. The focused beam is split, and the deflected portion of the beam bounces between two mirrors to increase the optical path so that we simultaneously capture a second intensity image at an out-of-focus plane. The beam splitter and the mirror are tilted slightly to create spatial separation between the in-focus and out-of-focus images. A neutral density filter is also placed in the path of the focused beam to compensate for the intensity difference between the two images.

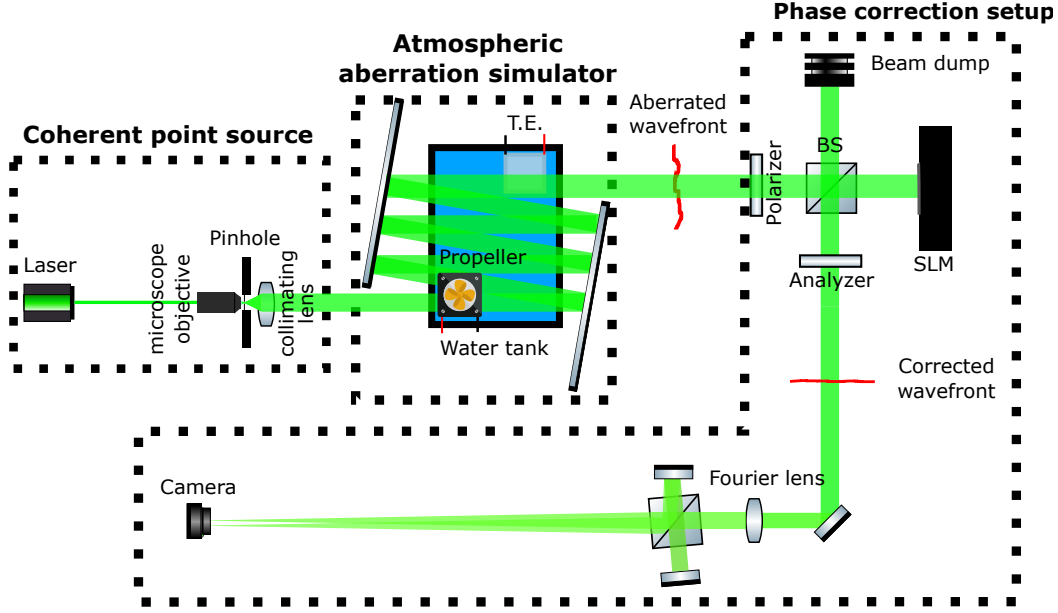


Figure 3. A prepared input beam is passed through an atmospheric aberration simulator. The resulting aberrated wavefront is passed on to the phase correction setup.

3.2 Experimental procedure

Instead of using numerical simulations as Tian et al. and Möckl et al.^{14,16} did, we created experimentally obtained data set for the training and evaluation of our network. At the data collection stage, the thermoelectric device and the water propeller are turned off. Following the procedure in Guo et al.,¹⁵ we addressed the SLM using generated aberration phase profiles subject to energy constraints. This directly generated aberrated intensity images used for our training and testing sets. An advantage of this approach is that it avoids potential disagreements between idealized simulations and imperfect experimental setups. An important difference between the system of Guo et al.¹⁵ and ours is that we can obtain images at two focal positions at the same time, which plays a key role when performing real-time aberration correction.

In real applications such as atmospheric aberration correction, phase profiles are not static. Therefore, as a next step, we utilized the SLM to simulate temporally varying atmospheric turbulence. Again, the estimated phase from the intensity at a given instant becomes inaccurate as the phase aberration changes. In addition, control theory needs to be considered as aberration correction interacts with the system. It is therefore important to examine the performance of the algorithm, experimentally, under temporally varying phase aberration.

So, finally, the algorithm is tested against actual physical turbulence aberration. Again, to generate observable turbulence, temporal density variation is created by adding salt to the water and turning on a thermoelectric device and water propeller.

4. RESULTS

4.1 Algorithm training results

100,000 pairs of images are acquired from displaying random aberration profiles onto the SLM. The neural network is trained for multiple epochs. To test the validity of the model, we examine the differences between newly generated (unseen by the network during training or validation) Zernike coefficients that cause aberration and their corresponding prediction results. The randomly generated phase profile is displayed on the SLM, and an image is then acquired and used to predict the aberration coefficients. The prediction result is subtracted from the generated coefficients to obtain the residue coefficients. These coefficients are used to compute the

residue phase aberration which is then displayed onto the SLM. A simulated corrected point spread function (PSF) is finally obtained by taking an image. Fig. 4a shows some snapshots of corrected and uncorrected PSFs.

To quantify the effects of aberration correction, we also compare the variances of the uncorrected Zernike coefficients and the residue coefficients after correction. Fig. 4b shows their variances. Variances are calculated from 100 randomly generated aberrations. A clear reduction in variance after aberration correction indicates the success of the model, and also illustrates that the correction is most effective for smaller Noll indices with larger variance.

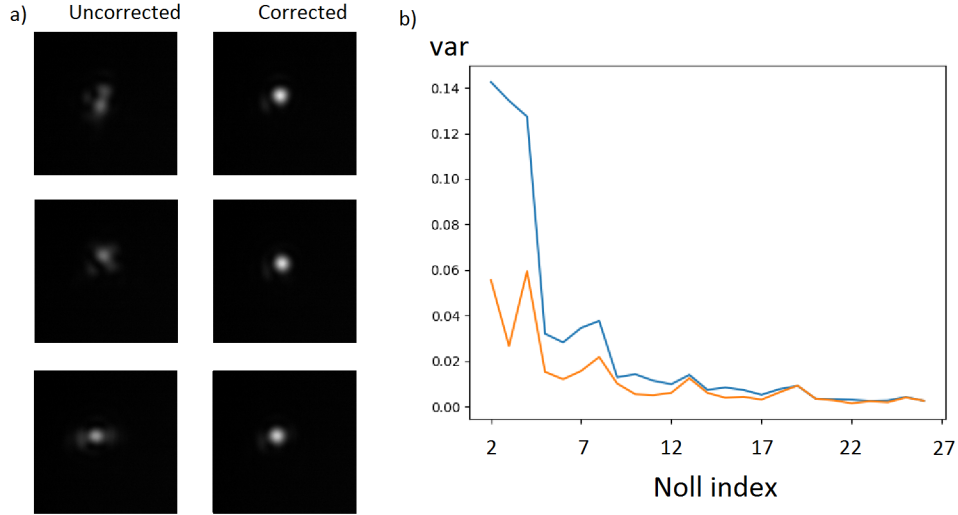


Figure 4. a) Some snapshots of uncorrected PSFs compared to corrected PSFs. b) Simulated variances of Zernike coefficients before and after aberration correction. The horizontal axis is the Noll index of Zernike polynomials, and the vertical axis is the variance of the polynomial coefficients. The blue line corresponds to the randomly generated coefficients, and the orange line corresponds to the residue of the coefficients after subtracting the prediction results.

4.2 Simulated aberration correction results

We examine the standard deviation of the PSF in pixels before and after aberration correction. To simulate temporally varying phase aberration, we generate temporally varying Zernike coefficients satisfying energy constraints as discussed earlier. Previous literature discussed using a random walk algorithm to generate temporal correlation between Zernike coefficients,^{22,23} and a simpler method of using the spline technique to connect random independent Karhunen-Loeve polynomials.²⁴ For our purposes, it is sufficient to simply accumulate the independently Gaussian distributed Karhunen-Loeve coefficients. In our simulation, we reduce the coefficients in the previous frame to 0.95 of its variance, and add a new set of coefficients with 0.05 of its variance. Choices of these parameters affect how rapidly evolving turbulence is relative to the correction rate. The resulting coefficients are slowly evolving and Gaussian distributed with a fixed variance across different frames. Aberration is measured in terms of standard deviations in pixels of the PSFs as shown in Fig. 5. The graph begins with the start of the algorithm when the PSF has a large spread. The algorithm very rapidly converged, to correct for the aberration.

4.3 Results on water turbulence aberrated PSFs

To perform real-time aberration correction, the update rate of correction phase profiles needs to be higher than the rate of change in turbulence. The camera acquisition time is around 20 ms per frame. With an NVIDIA GeForce GTX 750 Ti graphics card and an AMD FX-6300 six-core processor, the neural network prediction time is 10 ms and the phase profile GPU calculation time is 7 ms. Including all other computational steps, the time for each frame is about 50 ms. We have demonstrated a correction rate of 20 frames per second (fps), but

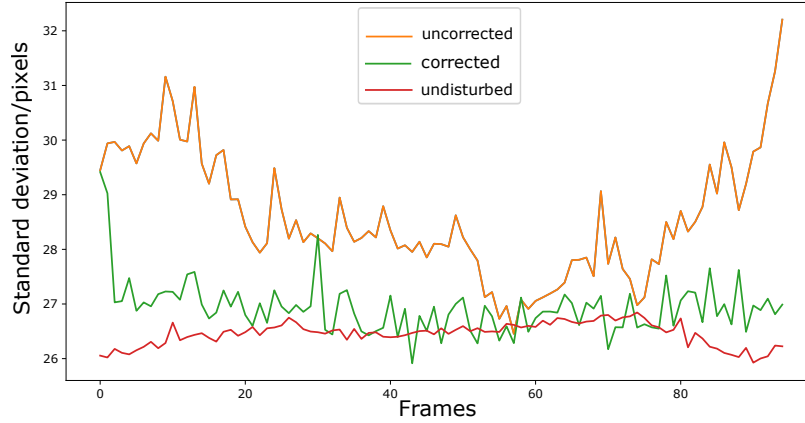


Figure 5. Standard deviation of PSFs before and after aberration correction. An undisturbed beam PSF standard deviation is shown for reference. The measurement of standard deviation for simulated aberration (this figure) is implemented slightly differently compared to that of real physical aberration (Fig. 6). The data is re-scaled to match that of the physical aberration.

the time constant of the liquid crystal solution within the SLM means that higher correction rates will be less effective.

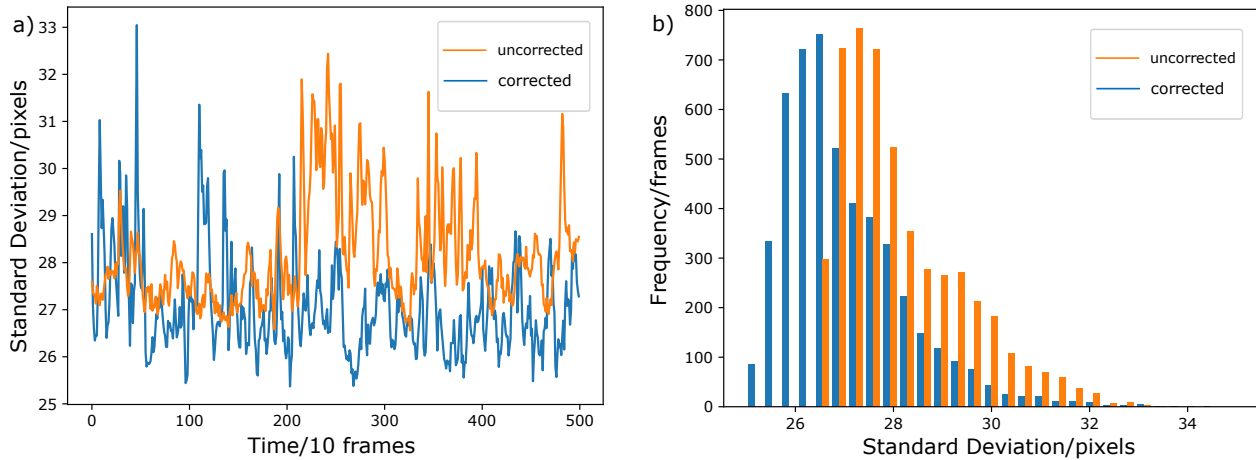


Figure 6. This figure shows data collected with water aberration. To obtain data both when correction is applied and not, two separate runs are used. Therefore, aberration between the two data sets is not temporally correlated. a) Time variation in beam width given by the standard deviation for corrected and uncorrected cases. Each data point is averaged over ten frames. b) Distribution of beam width: it can be seen clearly that the overall beam spread as a result of aberration is mitigated by applying the algorithm.

Fig. 6 shows the experimental performance of the aberration correction algorithm. Fig. 6a indicates that there is an overall reduction in the spread of the beam. Fig. 6b is a histogram of beam width, further confirming the aforementioned observation.

However, by examining the video files of the laser beam acquired under water aberration with and without correction, we find that the correction algorithm suffers from instability. Oscillatory behavior is clearly observed where the algorithm overcorrects. This is a consequence of the delay of SLM response. On average, it takes 4 frames for the SLM to fully change to a new configuration. This reduces the effective aberration correction rate significantly, and limits the performance of the algorithm. Better image displaying, SLM addressing and camera acquisition synchronization, as well as faster hardware, should address the problem. The simple inclusion of

a differential term does not solve this problem effectively, possibly because incorrect estimates of the Zernike coefficients get amplified in this algorithm.

5. CONCLUSION

We demonstrated that the neural network-based technique for wavefront correction works on real physical systems. However, there are several drawbacks that we encountered during the evaluation of the network on physical systems.

The first challenge is the spatial intensity variation of the beam on the SLM active area. Aberration happens before the SLM plane, and the complex optical field can have amplitude variations upon arriving to the SLM plane. The training set of the algorithm assumes no intensity variation and hence cannot take this fact into account. This can lead to incorrect estimates of Zernike coefficients since the resulting Fourier transform observed by the camera would be affected by this variation, and possibly worsen the phase profile in the end. Algorithms using the Shack-Hartmann wavefront sensor⁴ directly measure the wavefront and do not suffer from this problem. Other wavefront-sensorless algorithms such as the stochastic parallel gradient descent (SPGD)⁵ are feedback based and do not make direct guesses of Zernike coefficients, hence are unaffected by this issue as well. Including this effect in the training set, using more images at different focal positions and merging the algorithm with a model-free search algorithm might mitigate this drawback.

The second challenge in real applications lies in increasing the frame rate even further since atmospheric turbulence evolves much faster. By acquiring smaller pictures and using a faster CPU, GPU, camera, and SLM, a moderate speed up can be achieved. Better synchronization between the computer, SLM and camera is critical as well. Deploying the algorithm to a binary executable can also contribute. Previous literature also implemented a deconvolutional neural network that outputs phase profiles directly, skipping the step of computing the profile from Zernike polynomials altogether.¹⁵ The advantages of this architecture are shorter computation time and a smaller inaccuracy due to truncation of high order Zernike polynomials.

The third challenge is the stability of the correction algorithm. Incorrect estimation leads to an increase in distortion. Unlike in control problems where the error is a scalar (e.g. temperature, position), the estimation of a correction vector is harder, and summing incorrect estimates to the integral term leads to a lasting effect. Moreover, the statistics of the remaining wavefront after correction might be different from the uncorrected wavefront, which means a different training set should be used for optimal behavior of the network. The residual statistics could depend on the ratio of the rate of correction and the time scale of temporal turbulence variation. An iterative process of training a network and simulating its residual and training another network for the residual could be used to eventually find a network with comparable statistics before and after correction. Working only with Karhunen-Loeve coefficients as the output of the network might be desirable in order to avoid dealing with cross-correlations between coefficients.

The fourth challenge is the deployability of the model to different physical systems. The algorithm is trained in a specific situation, and is sensitive to small variations in data selected. Imperfections in the optical systems and the brightness and width of received beams are all fixed during the training process. Out of focus intensity images are especially sensitive to variations between physical setups, and that gives a reason to use fewer images at different focal positions. Slight alterations in these characteristics result in an unusable algorithm. Augmentation of the training set is necessary to improve the generalizability of the neural network, possibly by intensity and beam size variations through normalization and rescaling of images.

REFERENCES

- [1] Liang, J., Williams, D. R., and Miller, D. T., "Supernormal vision and high-resolution retinal imaging through adaptive optics," *J. Opt. Soc. Am. A* **14**, 2884–2892 (Nov 1997).
- [2] Roddier, F., "Curvature sensing and compensation: a new concept in adaptive optics," *Appl. Opt.* **27**, 1223–1225 (Apr 1988).
- [3] Hardy, J. W. and Thompson, L., "Adaptive optics for astronomical telescopes," *Physics Today* **53**, 69 (April 2000).

- [4] Moreno-Barriuso, E. and Navarro, R., "Laser ray tracing versus hartmann–shack sensor for measuring optical aberrations in the human eye," *J. Opt. Soc. Am. A* **17**, 974–985 (Jan 2000).
- [5] Vorontsov, M. A., Carhart, G. W., Cohen, M., and Cauwenberghs, G., "Adaptive optics based on analog parallel stochastic optimization: analysis and experimental demonstration," *J. Opt. Soc. Am. A* **17**, 1440–1453 (Aug 2000).
- [6] Weyrauch, T. and Vorontsov, M. A., "Atmospheric compensation with a speckle beacon in strong scintillation conditions: directed energy and laser communication applications," *Appl. Opt.* **44**, 6388–6401 (Oct 2005).
- [7] Zommer, S., Ribak, E. N., Lipson, S. G., and Adler, J., "Simulated annealing in ocular adaptive optics," *Opt. Lett.* **31**, 939–941 (Apr 2006).
- [8] Yang, P., Ao, M., Liu, Y., Xu, B., and Jiang, W., "Intracavity transverse modes controlled by a genetic algorithm based on zernike mode coefficients," *Opt. Express* **15**, 17051–17062 (Dec 2007).
- [9] Yin, X., Chang, H., Cui, X., Ma, J.-X., Wang, Y.-J., Wu, G.-H., Zhang, L., and Xin, X., "Adaptive turbulence compensation with a hybrid input-output algorithm in orbital angular momentum-based free-space optical communication," *Appl. Opt.* **57**, 7644–7650 (Sep 2018).
- [10] Booth, M. J., "Wavefront sensorless adaptive optics for large aberrations," *Opt. Lett.* **32**, 5–7 (Jan 2007).
- [11] Facompres, A., Beaurepaire, E., and Débarre, D., "Accuracy of correction in modal sensorless adaptive optics," *Opt. Express* **20**, 2598–2612 (Jan 2012).
- [12] Song, H., Fraanje, R., Schitter, G., Kroese, H., Vdovin, G., and Verhaegen, M., "Model-based aberration correction in a closed-loop wavefront-sensor-less adaptive optics system," *Opt. Express* **18**, 24070–24084 (Nov 2010).
- [13] Cybenko, G., "Approximation by superpositions of a sigmoidal function," *Math. Control Signal Systems* **2**, 303–314 (Dec 1989).
- [14] Tian, Q., Lu, C., Liu, B., Zhu, L., Pan, X., Zhang, Q., Yang, L., Tian, F., and Xin, X., "Dnn-based aberration correction in a wavefront sensorless adaptive optics system," *Opt. Express* **27**, 10765–10776 (Apr 2019).
- [15] Guo, H., Xu, Y., Li, Q., Du, S., He, D., Wang, Q., and Huang, Y., "Improved machine learning approach for wavefront sensing," *Sensors* **19**, 3533 (Aug 2019).
- [16] Möckl, L., Petrov, P. N., and Moerner, W. E., "Accurate phase retrieval of complex 3d point spread functions with deep residual neural networks," *Applied Physics Letters* **115**(25), 251106 (2019).
- [17] Tyson, R., [*Principles of Adaptive Optics*], Series in Optics and Optoelectronics, CRC Press (2010).
- [18] Noll, R. J., "Zernike polynomials and atmospheric turbulence*," *J. Opt. Soc. Am.* **66**, 207–211 (Mar 1976).
- [19] Fried, D. L., "Statistics of a geometric representation of wavefront distortion," *J. Opt. Soc. Am.* **55**, 1427–1435 (Nov 1965).
- [20] Roddier, N. A., "Atmospheric wavefront simulation using Zernike polynomials," *Optical Engineering* **29**(10), 1174 – 1180 (1990).
- [21] Ellerbroek, B. and Rhoadarmer, T., "Adaptive wavefront control algorithms for closed loop adaptive optics," *Mathematical and Computer modelling* **33**(1-3), 145–158 (2001).
- [22] Putnam, I. B. and Cain, S. C., "Temporally Evolving Atmospheric Phase Screen Generation," in [*Advanced Maui Optical and Space Surveillance Technologies Conference*], 5 (Sept. 2012).
- [23] Richmond, R. D. and Cain, S. C., [*Direct-Detection LADAR Systems*], SPIE Press, Bellingham (2010).
- [24] Wilcox, C. C. and Restaino, S. R., "A new method of generating atmospheric turbulence with a liquid crystal spatial light modulator," in [*New Developments in Liquid Crystals*], Tkachenko, G. V., ed., ch. 4, IntechOpen, Rijeka (2009).

© (2020) COPYRIGHT Society of Photo-Optical Instrumentation Engineers (SPIE). Downloading of the abstract is permitted for personal use only.

Minzhao Liu, David N. Lopez, and Gabriel C. Spalding "Experimental implementation of wavefront sensorless real-time adaptive optics aberration correction control loop with a neural network", Proc. SPIE 11469, Emerging Topics in Artificial Intelligence 2020, 114691S (20 August 2020); <https://doi.org/10.1117/12.2569647>